Range expansions transition from pulled to pushed waves as growth becomes more cooperative in an experimental microbial population

Saurabh R. Gandhi[1], Eugene Yurtsev[1], Kirill S. Korolev[2*], Jeff Gore[1*]

[1] Physics of Living Systems Group, Department of Physics, Massachusetts Institute of Technology, Cambridge, MA 02139, USA

[2] Department of Physics and Graduate Program in Bioinformatics, Boston University, Boston MA, 02215, USA

[*]Corresponding authors: [2]korolev@bu.edu, [1]gore@mit.edu

Supplementary Information Appendix

1. Reaction-diffusion models for one-dimensional range expansions

Populations expanding via short-range migration in one spatial dimension are often modeled by a reaction-diffusion equation, which is continuous in space and time:

$$\frac{\partial n}{\partial t} = D\frac{\partial^2 n}{\partial x^2} + nr(n). \qquad \text{S1}$$

Here *n(x,t)* is the density of population at position *x* at time *t*; *D* is the dispersal coefficient, which is assumed to be constant in the simple model, and $r(n)$ is the density-dependent per capita growth rate of the population. Many properties of this model can be obtained analytically by linearizing the growth term, $nr(n) \approx nr(0)$ at low densities (Fig. S1); we will also denote $r(0)$ as r_0. When colonization dynamics are determined by the dynamics at the expansion edge, this approximation is quite accurate because population densities are low at the expansion front. Kolmogorov *et. al.* proved that, when $r(n)$ is a monotonically decreasing function, this linearization is guaranteed to capture the expansion dynamics (55). Expansions described by the linearized growth term are called pulled because they advance via growth at the low-density front, which effectively pulls the waves forward. Importantly, the condition derived by Kolmogorov *et. al.* is sufficient but not necessary. In particular, the linear approximation continues to hold even when a small Allee effect is present. For larger Allee effects, dispersal from the faster growing high density region of the front dominates the growth at the low-density expansion edge, effectively pushing the wave forward. These 'pushed' waves advance at a higher velocity than one would predict using just $r(0)$ (17).

Although the model (eqn. S1) can be analyzed in numerous ways (17, 18, 24), a solution using Fourier transforms is most useful for extending the results to the case of discrete space and time systems, such as in our experiments. Here, we briefly outline the solution to the continuous model using Fourier modes as described by van Saarloos (17). We then apply a similar analysis to a model appropriate for our experimental system, which was used to predict the linearized-growth-velocities in the main text.

The spatial Fourier modes of the front can be written as:

$$\tilde{n}(q,t) = \int_{-\infty}^{\infty} dx n(x,t) e^{-iqx} \qquad \text{S2}$$

where q is the wave number of the Fourier modes. To obtain the spreading speed of a front, we start with an Ansatz assuming the Fourier modes are of the form $\tilde{n}(q,t) = \tilde{n}(q)e^{-i\omega(q)t}$. Substituting back in eqn. S1 gives the dispersal relationship ($\omega(q) = i(r_0 - Dq^2)$). Assuming that the front moves with some constant asymptotic velocity, v^*, we perform inverse Fourier transforms in the coordinate frame moving with the front ($\zeta = x - v^*t$):

$$n(\zeta,t) = \frac{1}{2\pi}\int_{-\infty}^{\infty} dq\; e^{iq\zeta - i[\omega(q) - v^* q]t} \qquad \text{S3}$$

In the large time limit, only those modes near the saddle point of $[\omega(q) - v^*q]$ survive (60), which results in the following condition:

$$v^* = \left.\frac{d\omega}{dq}\right|_{q^*} \qquad \text{S4}$$

where q^* is the saddle point. Further, in the co-moving reference frame, the wave profile neither grows nor decays in time, so the imaginary part of the exponent must vanish:

$$Im\big(\omega(q^*)\big) - Im(q^*)v^* = 0 \qquad \text{S5}$$

This gives the set of relationships that can be used to calculate the asymptotic velocity:

$$v^* = \left.\frac{Im(\omega(q))}{Im\,(q)}\right|_{q^*} = \left.\frac{d\omega}{dq}\right|_{q^*} \qquad \text{S6}$$

The above two relationships uniquely determine the asymptotic speed v and q^*. The exponential decay rate of the population density at the front then follows eqn. S3 since $\lambda = Im\ (q^*)$. The results are

$$v^* = 2\sqrt{r_0 D},\ \lambda = \sqrt{\frac{r_0}{D}}\ \ . \qquad \text{S7}$$

2. *Expansions in discrete space and time models*

The discretized form (corresponding to the experimental protocol) of the F-KPP equation can be written as:

$$n_{x,t+\Delta t} = g_{\Delta t}\left(n_{x,t} + \frac{m}{2}\left(n_{x+\Delta x,t} + n_{x-\Delta x,t} - 2n_{x,t}\right)\right), \qquad \text{S8}$$

where x is the spatial coordinate, t is the cycle number, and $g_{\Delta t}(n)$ describes total growth rate, i.e. $g_{\Delta t}(n)$ is the product of the per capita growth rate and the population density. Upon linearization $g_{\Delta t}(n)$ can be written as:

$$g_{\Delta t}(n) = n\frac{e^{r_0\Delta t}}{dilution}, \qquad \text{S9}$$

which corresponds to exponential growth at rate r_0 followed by a dilution. Substituting the Fourier mode $\widetilde{n_x} = e^{iqx-i}$ in the above linearized equation gives the dispersion relation:

$$e^{-i\omega\Delta t} = \frac{e^{r_0\Delta t}}{dilution}\left[1 + m(cosh(-iqx) - 1)\right] \qquad \text{S10}$$

Following the analysis of the continuous case, we use the saddle point approximation and require that the front is not changing in the co-moving reference frame. The resulting equations are similar to eqn. S6 and can be recast in a simpler form with the definitions of two real parameters $\lambda = Im(q)$ and $s = Im(\omega)$ and an observation that these equations correspond to the requirement that

$$v = min_{\lambda>0}\left\{\frac{S}{\lambda}\right\};$$

compare to eqn. 3 in the main text.

For small Δt, one can analytically obtain corrections to the continuous results in eqn. S7 due to the discreteness of space. However, since in our experiments, $\Delta t \sim 4$ hrs, which is longer than the time scale set by the growth rate (~2 hrs), the velocity and spatial decay rate have to be evaluated by minimizing eqn. S10 numerically.

The magnitude of deviations between the continuous and discrete models are shown in Fig. S3. Note that the discrete dynamical equation describing the experiment is not the same as the discretized version of the F-KPP equation, which can be written as:

$$n_{x,t+\Delta t} = n_{x,t} e^{r_{0,eff}\Delta t} + D_{eff} \frac{\Delta t}{\Delta x^2} \left(n_{x+\Delta x,t} + n_{x-\Delta x,t} - 2n_{x,t}\right) \qquad \text{S11}$$

Comparing eqns. S9 and S11, the effective growth and diffusion rates in the continuous model should be expressed in terms of experimental parameters as follows:

$$r_{0,eff} = r_0 - \frac{ln(dilution)}{\Delta t}$$

$$D_{eff} = \frac{m}{2}\frac{\Delta x^2}{\Delta t}(1 + r_{eff}\Delta t) \qquad \text{S12}$$

($\Delta t = 4$ hr, $\Delta x = 1$ well). The effective parameters can then be used in continuous models to compare them to the discrete space-time experimental model and evaluate the magnitude of 'corrections' that are introduced due to the discretization.

The finite number of organisms per spatial patch also changes the velocity and spatial decay rate. Although stochastic effects obviously cause fluctuations in the velocity, the expectation value of the velocity is also reduced as compared to predictions that do not incorporate demographic stochasticity. The deviations have been shown to be of the order of $\frac{1}{\log^2 N}$, where N is the number of individuals per unit length, when space and time are continuous (54). Moreover, the fronts have been shown to be steeper when demographic stochasticity is added (53, 54). We see this in our experiments, where, without accounting for the demographic stochasticity, the observed spatial decay rate is larger than predicted. This discrepancy vanished when we incorporated the effects of stochasticity in our predictions (Fig. S4).

3. Cubic model of the Allee effect

A generic model of the Allee effect was used for making the cartoon in Fig. 4 in the main text. In this model, the density dependence of growth is given by:

$$\frac{1}{n}\frac{dn}{dt} = \frac{r_0}{a}\left(1 - \frac{n}{k}\right)(n + a) \tag{S13}$$

This model shows no Allee effect for $a > k$ (per capita growth rate monotonically decreases with increasing density), and a weak Allee effect for $a < k$. Further, as a is varied, the growth rate at low density remains constant and is given by r_0. The transition from pulled to pushed waves occurs at $a = k/2$ inside the weak Allee effect regime (64).

4. A mechanistic growth model captures the Allee effect and shows a transition from pulled to pushed waves with increasing sucrose

We developed a mechanistic model for yeast growth in our experiments. The model incorporates previously well-studied mechanisms such as Monod growth on glucose (61) and a Michaelis-Menten kinetics of sucrose hydrolysis (49, 52, 63). Using previously measured values of the model parameters (Table S1), we found that the magnitude of the Allee effect increases with the amount of sucrose in the medium. Importantly, the model also displayed a transition from pulled to pushed waves, consistent with the experimental observations in Fig. 5 (Fig. S7). This transition was observed for a wide range of model parameters and is a generic prediction of the model. To test for quantitative agreement between the model and the experiments, we fitted the parameters of the model to our independent measurements of the growth rates, and confirmed that the predicted velocities closely match experimental observations (Fig. S8).

The model describes growth of yeast in the presence of glucose and sucrose, and assumes that there are no other limiting resources. Furthermore, while glucose is metabolized directly by the yeast, sucrose needs to be hydrolyzed to monosaccharides before it can be utilized. Although sucrose is hydrolyzed to glucose and fructose, we treat these sugars equivalently and refer to the combined concentration of the monosaccharides as the glucose concentration (49). This hydrolysis reaction is catalyzed by an enzyme invertase produced by yeast cells. Most of the invertase stays attached to the cell surface resulting in higher rates of hydrolysis in the immediate vicinity of the cell and creating a local cloud of glucose in excess of the bulk glucose concentration. Thus, yeast cell benefit from both the glucose produced by themselves and from the glucose produced by their neighbors (49). These dynamics are captured by the following Monod growth law and glucose consumption equation:

$$\frac{1}{n}\frac{dn}{dt} = \frac{g_{loc}}{g_{loc}+k_g}\gamma_{max} \tag{S14}$$

$$\frac{dg}{dt} = -Y\frac{dn}{dt} + nV \tag{S15}$$

Here, the first equation describes cell division, where n is the cell density, g_{loc} is the local glucose concentration around each cell, k_g is the Michaelis-Menten constant for glucose utilization and γ_{max} is the maximum division rate. The second equation gives the corresponding rate of utilization of glucose (g), which is proportional to the division rate of the cells (the proportionality constant, Y, determines the carrying capacity of the population). The additional term, nV, corresponds to the production of glucose due to sucrose hydrolysis. The per capita rate of sucrose hydrolysis, V, is given by

$$V = v_s\frac{s}{s+k_s} = -\frac{1}{n}\frac{ds}{dt}, \tag{S16}$$

where s is the sucrose concentration, v_s is the maximum rate of sucrose hydrolysis, and k_s is the Michaelis-Menten constant. Finally, the local glucose concentration around the cell is the sum of the bulk glucose concentration, and the additional cloud of glucose due to the sucrose hydrolysis on the cell surface. The contribution of this cloud is proportional to the rate of sucrose hydrolysis, and thus

$$g_{loc} = g + g_{eff}V, \tag{S17}$$

where g_{eff} is the proportionality constant that accounts for the glucose escape through diffusion (49).

To infer model parameters, we measured growth rates in varying sucrose concentrations, and different cell densities. The growth rate measurements and the corresponding range expansions were carried out in 9 different media: 0.125% glucose, and 0.008% glu + varying amounts of sucrose.

Before we describe the specifics of how the model parameters were determined from the experimental data, it is important to discuss how each parameter contributes to the different aspects of the experimental data and demonstrate that the data contains sufficient information to constrain the model parameters. The yield parameter, Y, determines the number of cells that can be produced given a certain amount of glucose. For the growth rate measurements in pure glucose, Y therefore controls the population densities at which the growth rate precipitously drops to zero. We determined Y by fitting the model prediction to our growth measurement at high cell densities in 0.125% glucose (Fig. S9). The growth rate at low cell densities in pure glucose media is completely determined by γ_{max} and k_g, and our data contained sufficient information to infer these parameters because we had low-density growth rate measurements in pure glucose as well as in several sucrose concentrations that produced varying local concentrations of glucose as specified by eqn. S17. The low-density growth rates at different sucrose concentrations also depend on k_s and $v_s g_{eff}$; therefore, we could use our low-density measurements to infer four model parameters γ_{max}, k_g, k_s and $v_s g_{eff}$.

The dynamics at high population densities depend not only on the product of v_s and g_{eff}, but on the individual values of these parameters. In particular, higher values of v_s and lower values of g_{eff} (keeping their product fixed) result in a larger Allee effect and more cooperative growth because of the faster sucrose hydrolysis and greater sharing of glucose via diffusion away from the cell. Therefore the magnitude of the Allee effect at high sucrose concentration provided the last necessary constraint to determine all of the model parameters.

Instead of directly fitting to the entire data set simultaneously, we used a modular approach of fitting the growth dynamics at low-density and high-density separately. We also bootstrapped on our data to determine the uncertainty in model parameters and model predictions.

To obtain a set of low density growth parameters, we bootstrapped over the measured values of growth rates in each of the media, and fitted the parameters by minimizing the squared distance from the bootstrapped data using Python package scipy (curve_fit). All data at starting densities below OD 0.004 was included, as indicated in Fig. S10. However, all outliers more than 2.5 SD away from the mean, were excluded from the analysis. Moreover, growth was unusually slow in one of the measurements, in 0.003%

sucrose. This is the regime where the low-density growth rate is independent of sucrose concentration, since the concentration of sucrose is lower than that of glucose, which was 0.008%. Therefore, we excluded this particular condition while fitting the parameters. The bootstrapping procedure was repeated to obtain 100 sets of low-density growth parameters, γ_{max}, k_g, k_s and $v_s g_{eff}$. Out of these, a few iterations of the curve_fit routine did not converge on the fit, leaving 89 sets of parameters for downstream analysis. Fig. S11 shows the low-density growth rates that the model predicts for each of the parameter sets.

Next, for each of the 89 sets obtained above, we determined the individual parameters, v_s and g_{eff}, keeping the product constant. As noted earlier, the relative magnitudes of these two parameters control the magnitude of the Allee effect. Therefore, parameters v_s and g_{eff} were determined by minimizing the squared distance from growth rates at intermediate densities in 2%, 0.67% and 0.22% sucrose – the media that exhibit a substantial Allee effect. The sum of squared distance from all the data points in the selected regions of the cell densities was calculated for values of v_s ranging from 0.2 to 4 % OD^{-1}hr^{-1}, and the value of v_s minimizing the sum was chosen. These regions of cell densities were selected such that the growth rates increase with density (i.e. exhibit an Allee effect) and are summarized below:

2% sucrose: OD 5x10^{-3} to 2x10^{-1},

0.67% sucrose: OD 5x10^{-3} to 2x10^{1},

0.22% sucrose: OD 5x10^{-3} to 3x10^{-1}.

Table S1 shows a comparison between the previously reported values of the parameters for yeast, and the median parameter values that we have obtained by the procedure described above. The distribution of parameter values is shown in Fig. S12. Most of the fitted values were consistent with literature. The exception is g_{eff}, which is an order of magnitude larger than previously reported. However, this parameter depends strongly on the diffusion rate of glucose, such that slower diffusion leads to larger g_{eff}. Since the cells in our experiments are not being shaken (both during range expansions as well as in the experiments we performed to measure growth rates), most of the hydrolysis products remain in the vicinity of the cell, resulting in lower diffusion, and a larger g_{eff}. Other factors that affect g_{eff} such as genetic background, cell size, etc. could also contribute to the observed difference with previous measurements. The lack of mixing is also consistent with the slightly lower v_s that we estimate compared to literature, since the efficiency of hydrolysis is reduced.

These 89 parameter sets fit the observed growth rates well over the entire range of cell densities and sucrose concentrations as shown in Fig. S13.

We then simulated expansions using the mechanistic growth model and the 89 parameter sets obtained above. The simulations exactly follow the experiments, and have cycles of migration/dilution followed by growth, with eqn. S14-S17 giving the dynamics in the growth phase (Fig. S14, SI section 5, SI simulation code). The simulated velocities for each of the 89 parameter sets all show a transition from pulled to pushed waves with increasing sucrose concentration, and are distributed closely around experimentally observed velocities (Fig. S8).

The excellent agreement between the model and the experimental observations further supports our conclusions that the break-down of the theory of pulled waves at high sucrose concentrations is due to an increasing strength of the Allee effect makes yeast expand as a pushed wave.

5. Simulations

Stochastic simulations were performed for computing the rate of exponential density decay at the front as well as for testing the predictions of the mechanistic growth model. In the simulations, the expansions were allowed to proceed for longer times than in the experiment, so as to completely remove all transients. Expansions were typically simulated for 60 cycles across a sufficiently long landscape so that the waves do not reach its edge. The total carrying capacity in each spatial patch was the same as in the experiments.

The simulations reflect exactly the dynamics in our experiments (Fig. S14). The cells start with an exponential spatial density profile. For each cycle, logistic model (in simulations for calculating the exponent at the front) or the mechanistic growth model is integrated over a period of 4 hours to obtain the final population density in each well. Growth is thus deterministic in the simulations. At the end of the growth cycle, the number of cells is rounded off to the nearest integer. Binomial sampling is used to determine the number of cells that are transferred for the next cycle, taking into account the migration rate as well as the dilution rate. This step therefore accounts for the demographic fluctuations.

Finally, since growth in the mechanistic model explicitly depends on sugar concentrations, we also include the effects of sugar transfer due to migration and dilution in the simulations (Fig. S14).

Velocities in the simulations are calculated in the same way as experiments (Materials and Methods). A threshold density of 2000 cells per well and the location of the wavefront is defined as the position at which the profile crosses this threshold. Velocity is then calculated by obtaining a linear fit between the position and time.

Parameter	**Median**	**Literature**	**References**
Maximal growth rate on glucose, γ_{max} [hr^{-1}]	0.390	0.3 – 0.55 (0.39)	39, 49-51
K_M for growth on glucose, k_g [% w/v]	0.0019	0.002 – 0.003 (0.002)	63
K_M for sucrose hydrolysis, k_s [% w/v]	0.781	0.5 – 1.5 (0.8)	49, 61-62
Maximal sucrose hydrolysis rate, v_s [% OD^{-1} hr^{-1}]	0.833	2.4 (2.4)	49
Privatization parameter, g_{eff} [OD hr]	0.02	0.0015 (0.0015)	49
Yield on glucose, Y [% OD^{-1}]	0.057	– (0.07)	–

Table S1

The table shows a comparison between previously reported and median values of model parameters obtained by fitting the model to measured growth rates. Values in brackets under the literature column are used for the simulation in Figure S7.

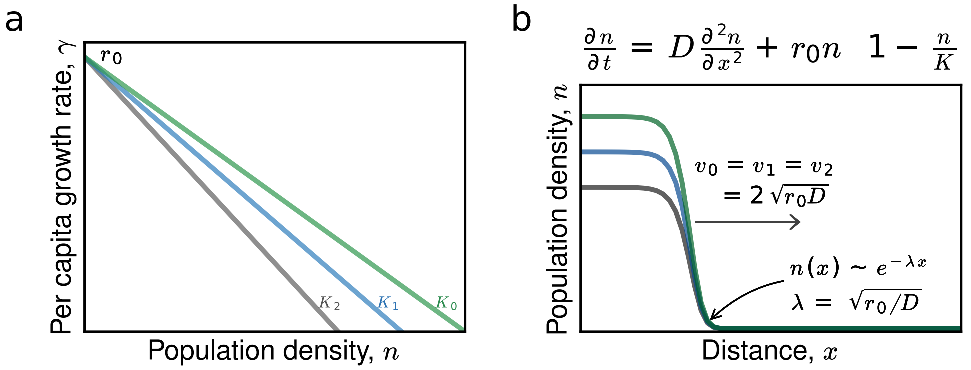

Figure S1

Reaction-diffusion equations are classical models for expansion in theoretical ecology. When populations grow logistically, Fisher's equation predicts traveling waves of constant velocity, with an exponential spatial profile near the front. Both of these emergent properties depend only on the low-density growth rate, and are independent of the carrying capacity.

(a) Populations that obey logistic growth increase exponentially with rate r_0 at low density, and the per capita growth rate decreases monotonically until the population density saturates at some carrying capacity, K. Three growth curves with identical low-growth rate, but different carrying capacities are shown. (b) Emergent properties of the expansion front, such as velocity (v) and spatial decay rate of density at the front (λ), depend only on the per capita growth rate at low density (r_0) and the diffusion constant (D), and are independent of the carrying capacity (v_0=v_1=v_2, λ_0=λ_1=λ_2=λ). The bulk density, however, does depend on the carrying capacity (K).

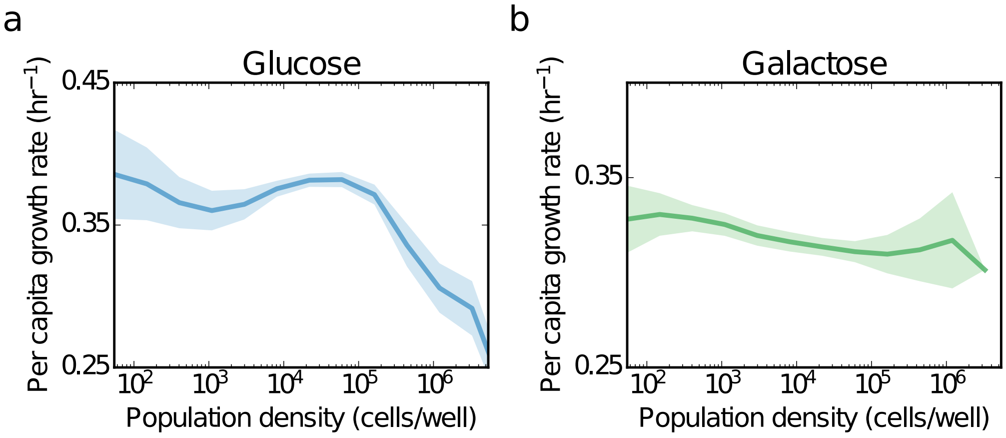

Figure S2

The maximal per capita growth rate in galactose (a) and glucose (b) never significantly exceeds the per capita growth rate at low density

We measured the fold growth by counting the number of yeast cells before and after 4 hours of growth in a 96-well plate. Each well started with a small number of yeast cells. After propagating the cultures with dilution for two 4-hour cycles (to remove transient effects caused by a change of growth environment), the number of cells in the wells were counted by flow cytometry at the beginning and end of the third and fourth cycle. Cells were counted after a 100x dilution. Due to the small numbers, the actual counts at low density had a large sampling noise. The figure shows the growth rate as an average over a Gaussian moving window. Shaded region indicates standard deviation in the average over the window in bootstrapped data. Since density does not change appreciably over the course of four hours, we estimated the growth rate assuming that it remains constant over the course of the experiment and results in an exponential increase in cell density.

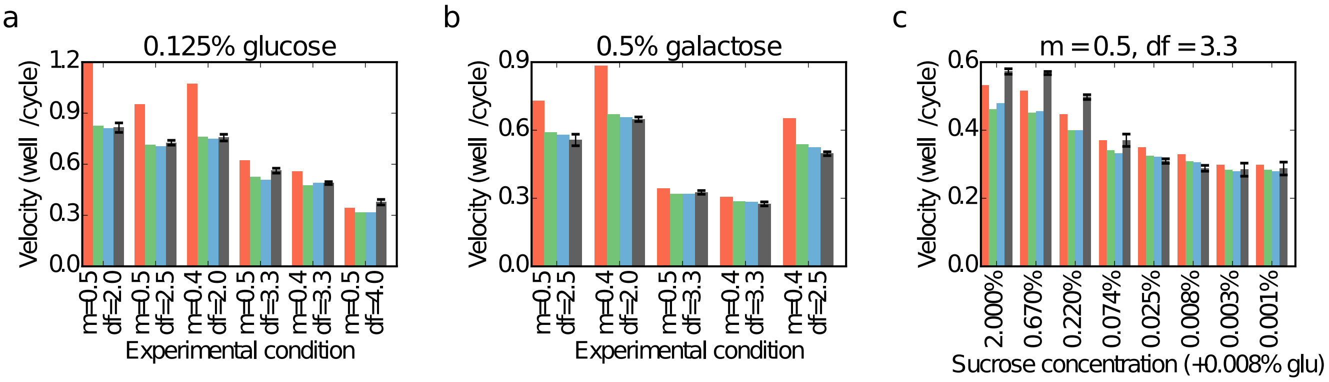

Figure S3

Effect of discretizing space and time (and addition of demographic stochasticity) on predicted velocities in glucose (a), galactose (b) and sucrose (c) environments. Each set of bars represents an experimental condition (different migration and death rates). In (c), the 8 conditions have constant migration and death rate, but decreasing amount of sucrose. Red bars indicate predicted linearized-growth-velocities in continuous space-time models with the same effective growth and diffusion rate as the discrete experimental system (eqn. S12). Here, we show a decomposition of the effects due to discrete space-time, and demographic stochasticity. Discreteness of space and time (green): Since migration is limited to one well at a time in the linear stepping stone model, emergent wave velocities can never exceed 1 well/cycle. The corrections are large and are calculated numerically from eqn. S10.

Demographic stochasticity (blue): Demographic stochasticity has been predicted to reduce expansion velocity. The correction to the continuous space-time model due to demographic stochasticity is of the order of $1/log^2(N)$. In our experiments, we calculated the corrections using simulations with measured growth rates and other known experimental parameters.

Experimental data (gray): We see that the observed velocities are in close agreement with predictions once the effects of discretization and stochasticity are incorporated (subplots a, b). Panel (c) shows that the observed and predicted velocities match for low but not high sucrose concentrations (even after incorporating the effects described above). The deviations are due to the large Allee effect at high sucrose concentrations, making the waves pushed. Error bars indicate S.D. in measured velocity at five different threshold densities.

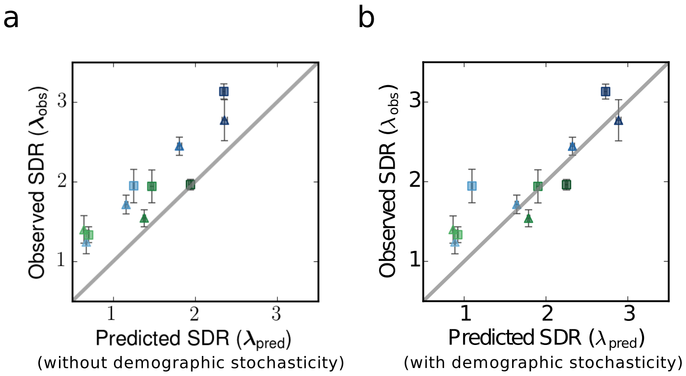

Figure S4

Demographic stochasticity significantly affects the spatial decay rate at the front (SI Section 2)

(a) Predicted spatial rate of decay at the front, based on linearized growth, is less than what is experimentally observed when demographic stochasticity is not taken into account. (b) When finite population effects (demographic stochasticity) are included, the observed front shape is close to predictions. The predicted spatial decay rate is based on simulations using measured values of low-density growth rate and known experimental parameters such as migration and death rate (SI section 5). y-axis error bars indicate S.D. in measured decay rate for three different fitting regions at the front.

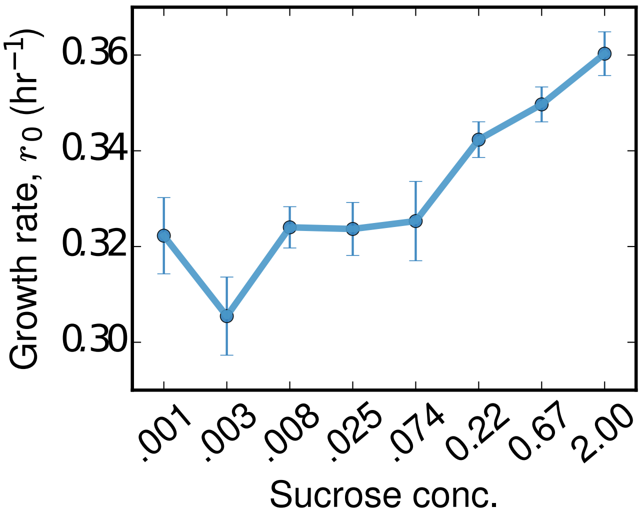

Figure S5
Low-density growth rate increases slowly with increasing sucrose concentration
Since some of the hydrolyzed sucrose is captured by the yeast cells before it can diffuse away, increasing the sucrose concentration leads to increased growth rates even at low densities, when cooperative effects are absent (SI section 4). However, the maximal growth rate increases faster than the low-density growth rate, resulting in an increasingly severe Allee effect (Fig. S6). Error bars indicate S.E.M. in measured low-density growth rates (Fig. S10).

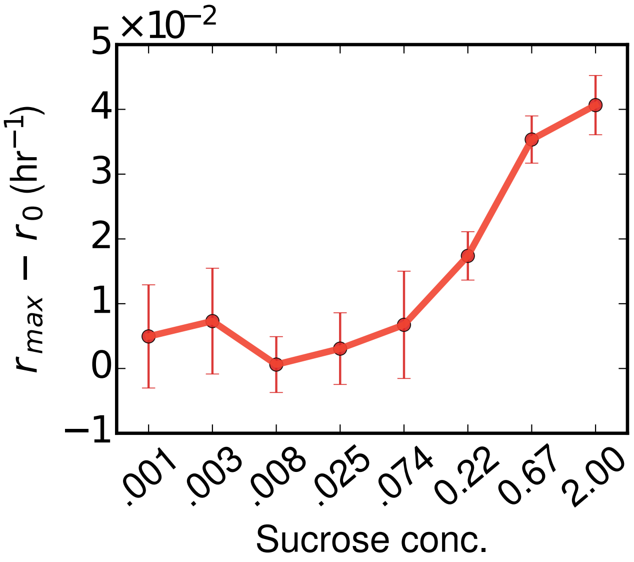

Figure S6
Magnitude of Allee effect increases with increasing sucrose concentration
The magnitude of the Allee effect is estimated as the difference between the maximal growth rate, r_{max}, and the low-density growth rate, r_0. Error bars indicate S.E.M. of the low-density growth rate (Δr_0). r_{max} was determined as the maximal value of the growth rate after averaging over a moving Gaussian window, as shown in Fig. S2 for 0.125% glucose and 0.5% galactose.

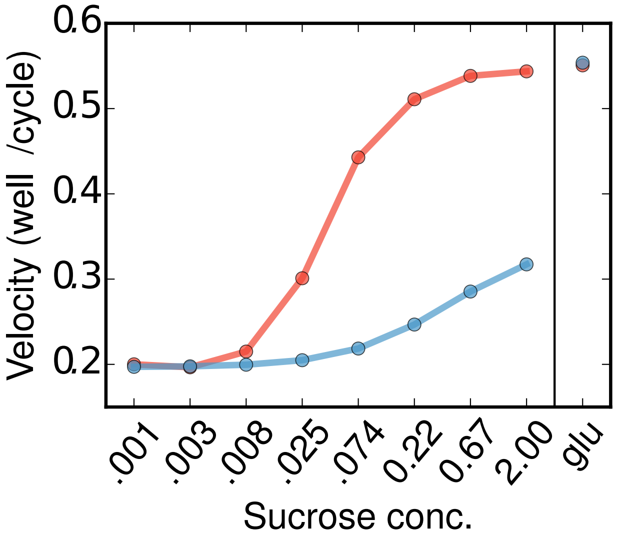

Figure S7
A mechanistic model of yeast growth on sucrose and glucose predicts a transition from pulled to pushed waves (SI section 4)
A simple mechanistic model where yeast grows on glucose following Monod kinetics, and hydrolyzes sucrose to glucose (details in SI) was used to simulate expansions. All the parameters in the model have been reported previously in various studies. Using typical parameter values from published literature (table S1), the model predicts a transition from pulled to pushed waves as the sucrose concentration in the media is increased. At low sucrose concentrations, expansions are pulled, reflected in the agreement between simulated velocities and the linearized-growth predictions. At larger sucrose concentrations, expansion velocities exceed the linearized-growth prediction, indicating that the expansions are pushed.

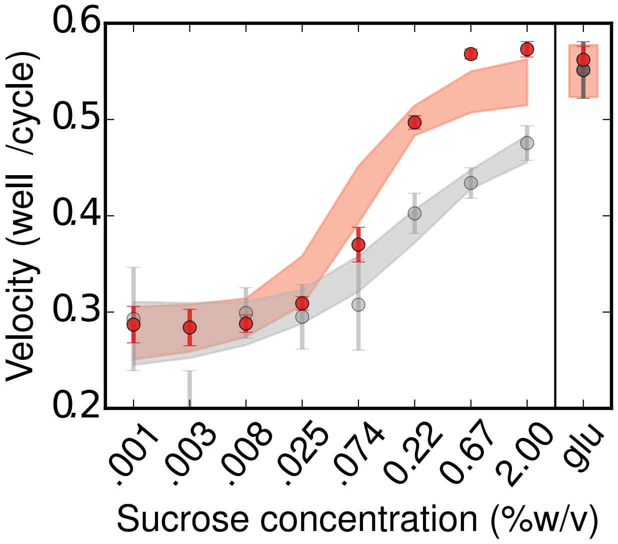

Figure S8
A mechanistic model for growth on glucose and sucrose predicts velocities close to what are observed experimentally (SI section 4)
Experimentally observed velocities in 8 different sucrose concentrations and in 0.125% glucose are shown as red points with SD errorbars. Gray points show the predicted linearized-growth velocities. Error bars are obtained by bootstrapping on the measured growth rates at low densities and calculating the linearized growth velocities. Shaded regions indicate predictions of the model. The observed velocities match well with the predictions of the model. The model also captures the transition from pulled to pushed waves as the deviation between observed and linearized-growth velocities (gray shading) around sucrose concentration of 0.025%. The width of the shaded regions is the standard deviation of simulation results for 89 parameter sets obtained by bootstrapping over the growth rate measurements and fitting the model to the bootstrapped data.

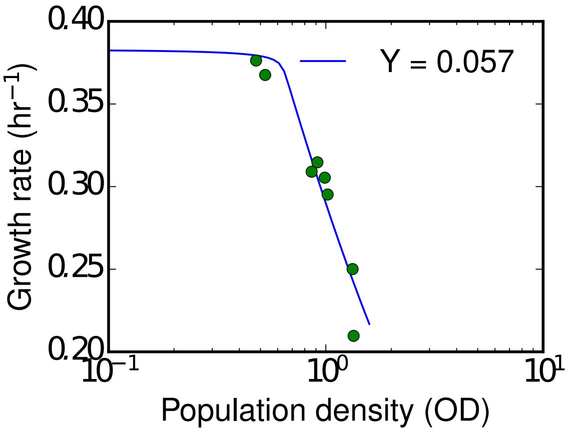

Figure S9
The yield parameter in the mechanistic model, Y, was obtained by fitting the model to growth rate measurements in 0.125% glucose, at high densities where there is a sharp decrease in growth rate with density. The yield parameter reflects the amount of glucose that a cell utilizes per division. At high cell densities, glucose is depleted quickly, causing the per capita growth rate to decrease sharply as starting OD is increased. By fitting the model to this region of growth, the value of Y can be determined accurately: Y = 0.057 OD^{-1}. Data is shown as green points, only at high densities, where growth rate is strongly affected by the yield parameter due to resource limitation.

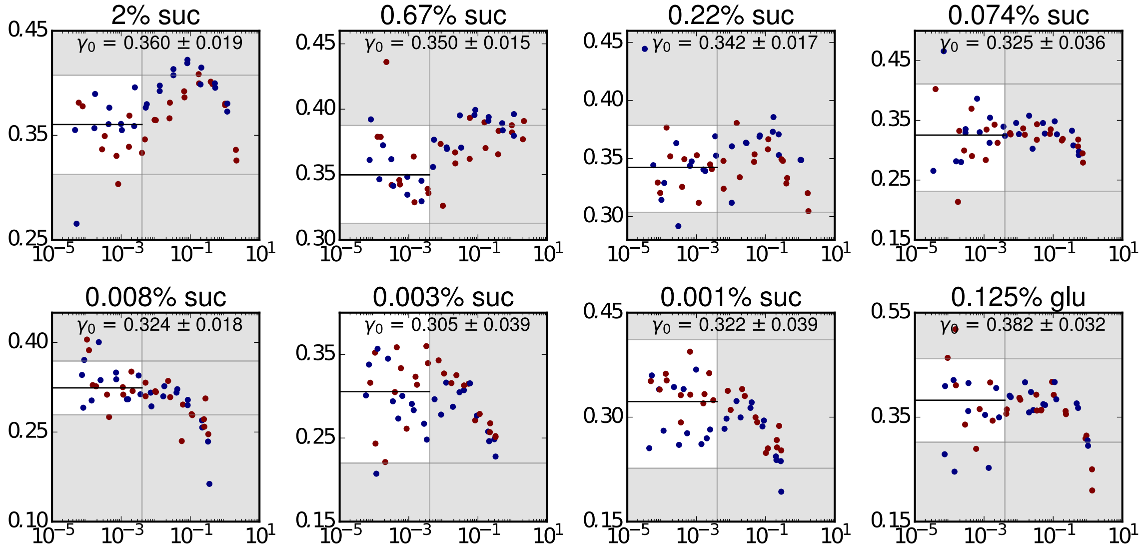

Figure S10
Low-density growth rates were measured by averaging the growth rate measurements over densities up to OD 0.004 (corresponding to 1000 cells per well). Population density is plotted along the x-axis, in terms of OD600, and growth rate is plotted along the y-axis for each panel. Data in the unshaded region is included as growth rate at low density. This region includes all data at ODs below 0.004 except for the outliers that are more than 2.5 SD away from the mean. Inset text indicates mean and S.E.M. of the unshaded data in hr^{-1}

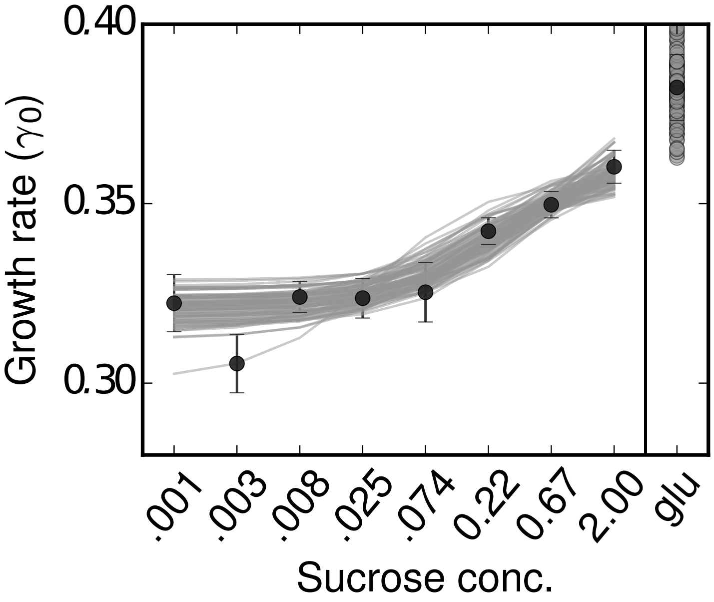

Figure S11

Low-density growth rates predicted across different sucrose concentrations by the model. We used 89 low-density parameter sets (γ_{max}, k_g, k_s, $v_s g_{eff}$) obtained by fitting to bootstrapped low-density growth rate measurements. Black circles with error bars represent the mean growth rate and s.e.m. Gray lines are model predictions. The details of the bootstrapping procedure can be found under section 4 in SI.

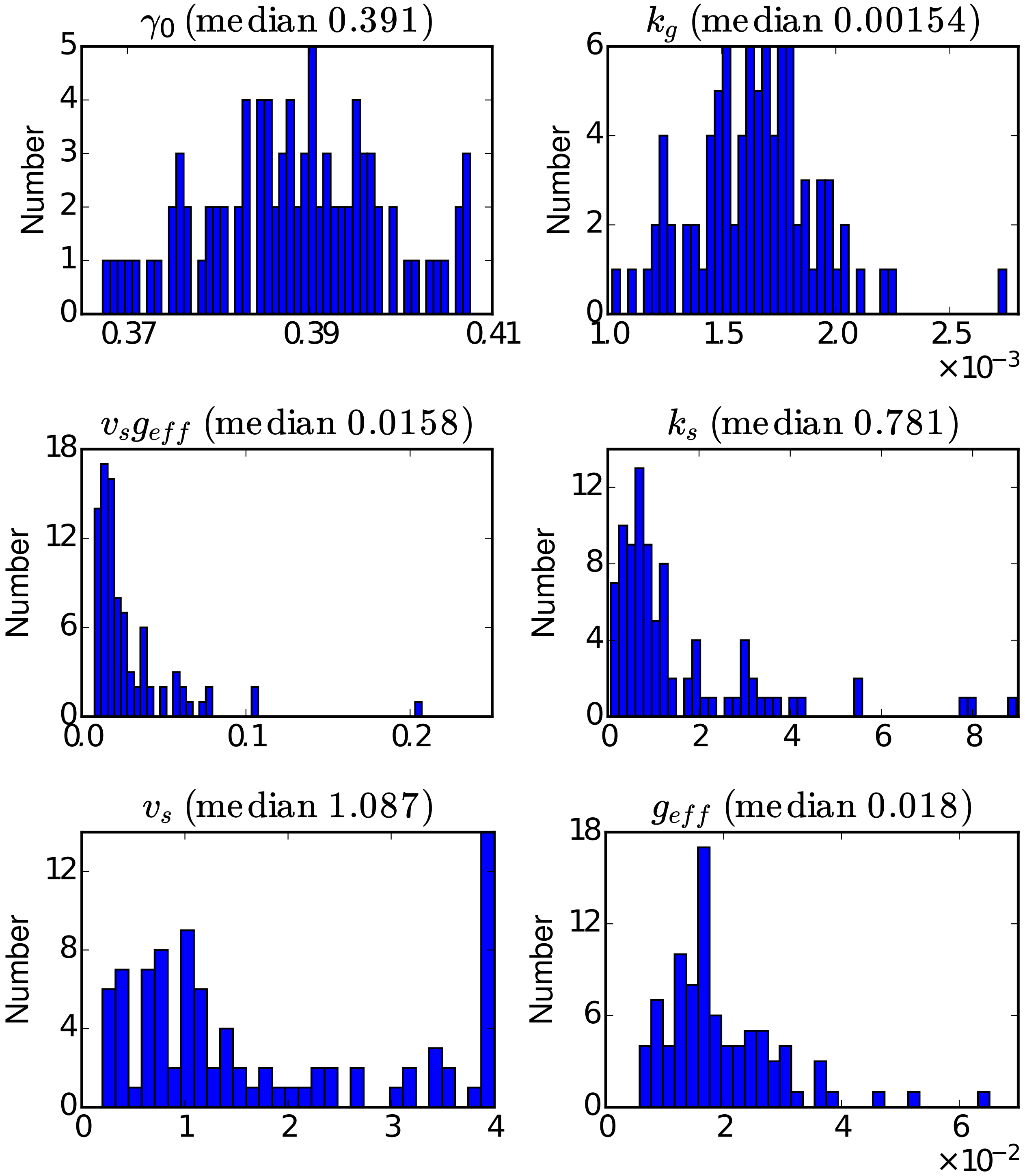

Figure S12

Distribution of parameter values in the 89 independent parameter sets obtained by bootstrapping over the data. Median values of the parameters are indicated in the title. Most median parameter values are in close agreement with previously reported values in the literature (Table S1). The exception is g_{eff}, which is expected to differ because the media is not shaken in our experiments (SI section 4).

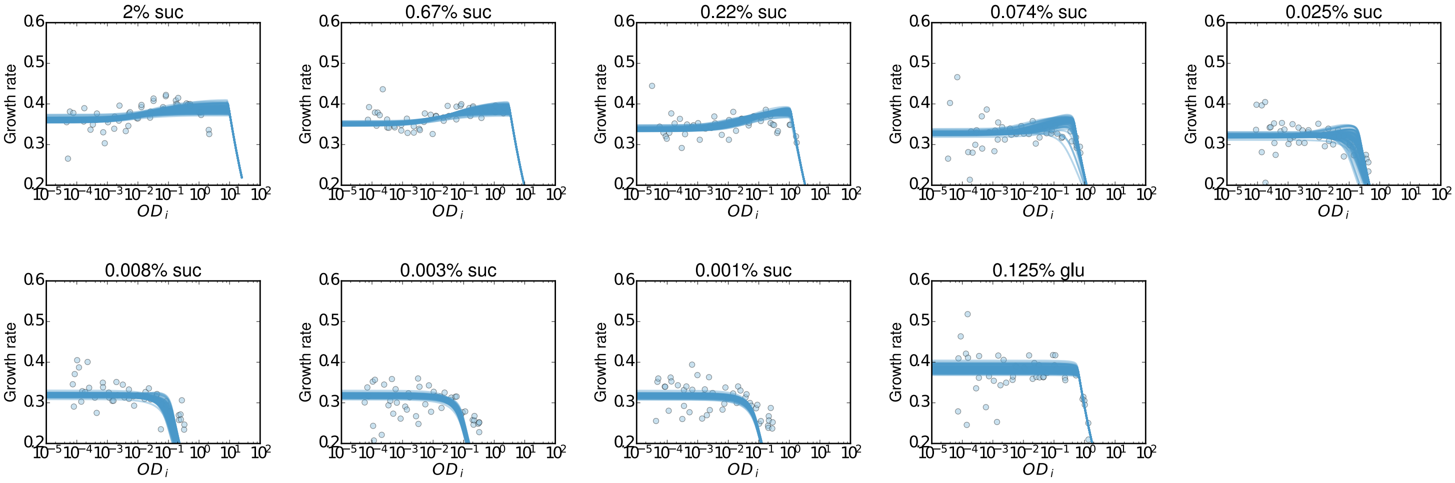

Figure S13

Allee effect increases with sucrose concentration. Measured growth rates at various cell densities are shown as blue points. Blue curves are the predictions of the model for each of the 89 parameter sets. For all parameter sets, the model matches the data well and shows an increasing Allee effect as sucrose concentration is increased.

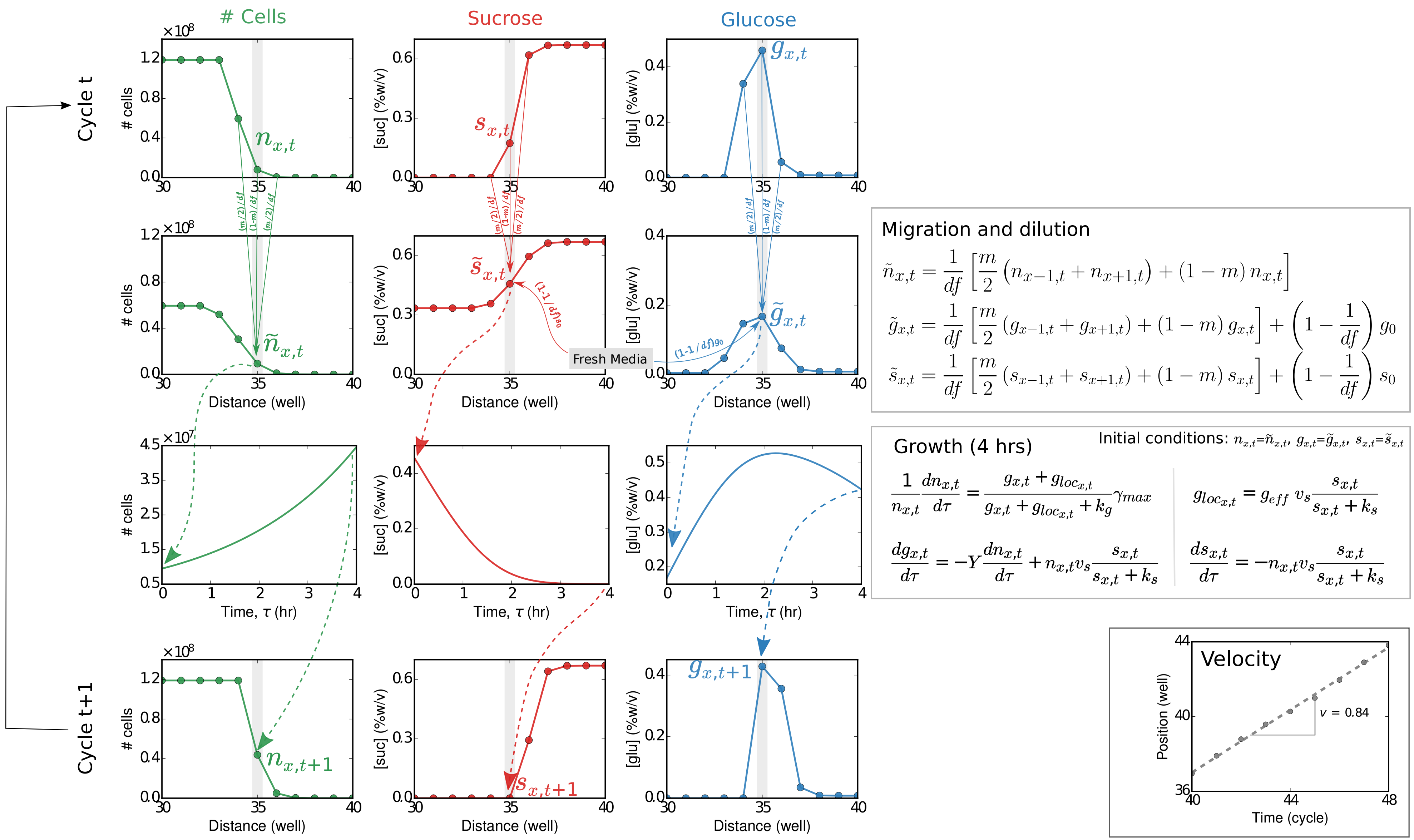

Migration and dilution

$$\tilde{n}_{x,t} = \frac{1}{df}\left[\frac{m}{2}\left(n_{x-1,t}+n_{x+1,t}\right)+(1-m)\,n_{x,t}\right]$$

$$\tilde{g}_{x,t} = \frac{1}{df}\left[\frac{m}{2}\left(g_{x-1,t}+g_{x+1,t}\right)+(1-m)\,g_{x,t}\right]+\left(1-\frac{1}{df}\right)g_0$$

$$\tilde{s}_{x,t} = \frac{1}{df}\left[\frac{m}{2}\left(s_{x-1,t}+s_{x+1,t}\right)+(1-m)\,s_{x,t}\right]+\left(1-\frac{1}{df}\right)s_0$$

Growth (4 hrs)

Initial conditions: $n_{x,t}=\tilde{n}_{x,t}$, $g_{x,t}=\tilde{g}_{x,t}$, $s_{x,t}=\tilde{s}_{x,t}$

$$\frac{1}{n_{x,t}}\frac{dn_{x,t}}{d\tau} = \frac{g_{x,t}+g_{loc_{x,t}}}{g_{x,t}+g_{loc_{x,t}}+k_g}\gamma_{max}$$

$$g_{loc_{x,t}} = g_{eff}\,v_s\frac{s_{x,t}}{s_{x,t}+k_s}$$

$$\frac{dg_{x,t}}{d\tau} = -Y\frac{dn_{x,t}}{d\tau}+n_{x,t}v_s\frac{s_{x,t}}{s_{x,t}+k_s}$$

$$\frac{ds_{x,t}}{d\tau} = -n_{x,t}v_s\frac{s_{x,t}}{s_{x,t}+k_s}$$

Figure S14
The figure shows how the density of cells and sugar concentrations as a function of space change over a cycle, in the simulation (SI section 5), following the dynamics in a single well highlighted above. At the end of cycle t, the cell density has a certain spatial profile (row 1). At the beginning of cycle t+1, cells are then diluted (by the factor df), and at the same time, a small fraction (m/2) is transferred to the neighbouring wells (row 2). The exact factor by which the densities change is illustrated next to the arrows from row 1 to row 2. The residual glucose and sucrose in the wells is also transferred over along with the cells. The fresh media into which the cells are diluted contains additional sugars (concentration s_0, g_0) for the cells to grow. Concentrations and cell densities at this intermediate step are denoted by $\tilde{n}$, $\tilde{g}$, $\tilde{s}$. The cells are then allowed to grow for 4 hours (row 3). In the simulations, the density at the end of 4 hours is obtained by integrating the growth model starting from the intermediate densities. Time within the growth phase is denoted by τ. The mechanistic model of growth, involving the cell densities as well as the sugar concentrations, is illustrated on the right. The profile at time t+1 is obtained at the end of growth (row 4), and the entire cycle of dilution/migration and growth is repeated. As can be seen, after the completion of a cycle, the profile is shifted in space. At a given time, t, the exact position of the wave is defined by the position at which the density profile crosses a certain threshold value (2000 cells, in the simulations). The velocity of expansion is given by the distance by which the profile shifts, averaged over multiple cycles (bottom right).

```
# Growth cycle integration
def grow(N, G, S, **kwargs):
    '''
    Takes into account the glucose and sucrose transferred over
    '''
    pars = kwargs['growth_params']
    model = kwargs['model']
    Nf, gf, sf = [], [], []
    for i in range(len(N)):
        n, g, s = N[i], G[i], S[i]
        concs = integrator(array([n, g, s]), 4, model, pars, res=0.01)[0].T
        Nf.append(concs[0][-1])
        gf.append(concs[1][-1])
        sf.append(concs[2][-1])
    return array(Nf), array(gf), array(sf)

# Final routine for each cycle
def simulate_expansion(**kwargs):
    num_cycles = kwargs['cycles']
    num_patches = len(kwargs['N_connected'])
    #dsc = kwargs['dscz']
    Npop = zeros((num_cycles, num_patches)) # Preallocate memory for the simulation
    glu, suc = ones((num_cycles, num_patches))*kwargs['g'], ones((num_cycles, num_patches))*kwargs['s']
    Npop[0] = array(kwargs['N_connected']) # Initialize the first row

    # Run simulation for num cycles
    for i in range(1, num_cycles):

        # Migrate
        Npop[i] = simulation2.discretize(simulation2.migrate(Npop[i-1], kwargs['m'], **kwargs), 1)
        df = kwargs['dilution_factor']
        m = kwargs['m']
        gSize = len(glu[i-1])
        left = arange(-1, gSize - 1) % gSize
        right = arange(1, gSize + 1) % gSize
        glu[i] = (1.-1./df)*glu[i] + 1./df*((1-m)*glu[i-1]+m/2.*(glu[i-1][left] + glu[i-1][right]))
        suc[i] = (1.-1./df)*suc[i] + 1./df*((1-m)*suc[i-1]+m/2.*(suc[i-1][left] + suc[i-1][right]))

        # Run Growth cycle
        Npop[i], glu[i], suc[i] = grow(Npop[i]/od_scale/volume, glu[i], suc[i], **kwargs)
        Npop[i] = simulation2.discretize(Npop[i]*od_scale*volume, 1)

    if 'ret_all' in kwargs.keys():
        return Npop, glu, suc
    return Npop

# Parameters
def gen_pardict(cycles=60, size=45, m=0.5, df=2, migrate='s', dilute='s', g=0.125, s=0,
                growth_pars=(0.39, 0.0019, 0.02, 0.057, 0.833, 0.781), model=jg2):
    par_dict = {
        'cycles' : cycles,
        'N_connected' : r_[zeros(size)],
        'm' : m,
        'dilution_factor' : df,
        'migrate' : migrate,
        'dilute' : dilute,
        'g' : g,
        's' : s,
        'growth_params' : growth_pars,
        'model' : model
    }
    par_dict['N_connected'][0] = 0.9
    par_dict['N_connected'][1] = 0.9
    par_dict['N_connected'][2] = 0.09
    par_dict['N_connected'][3] = 0.009
    par_dict['N_connected'][4] = 0.0009
    par_dict['N_connected'][5] = 0.00009
    par_dict['N_connected'][6] = 0.000009
    par_dict['N_connected'][7] = 0.0000009
    par_dict['N_connected'][8] = 0.00000009
    par_dict['N_connected'][9] = 0.000000009
    par_dict['N_connected'] = array(par_dict['N_connected']*od_scale*volume, int)
```

```python
    return par_dict

def integrator(v_i, t, model, params, res=0.001):
    n = int(t/res)
    arr = zeros((n, len(v_i)))
    tarr = zeros(n)
    arr[0] = v_i
    for i in range(1, n):
        arr[i] = arr[i-1] + model(arr[i-1], n*res, 0, *params)*res
        arr[i][where(arr[i] < 0)] = 0
        tarr[i] = i*res
    return arr, tarr

# Growth model
def jg2(v, t, verb, gamma, kappa, geff, alpha, beta, ks):
    '''
    1. Monod growth on glucose, with some background concentration of
       glucose (preferential access to hydrolyzed sucrose/diffusion,
       now proportional to rate of sucrose hydrolysis)
    2. Glucose is absorbed at a rate proportional to the division rate
    3. Michaelis-Menten sucrose hydrolysis
    '''
    n, g, s = v
    ds = -n*beta*s/(s+ks)
    gloc = geff*beta*s/(s+ks)
    dn = n*gamma*(g+gloc)/(g+gloc+kappa)
    dg = n*beta*s/(s+ks) - alpha*dn

    if verb:
        print 'dn/dt: %.3f OD/hr, dg/dt: %.3f%%/hr, ds/dt: %.3f%%/hr, g_loc: %.4f%%'%(dn, dg, ds, gloc)

    return array([dn, dg, ds])

# Calculating velocities using a threshold
def gen_velocities(gpars, opops={}, model=jg2, thresh=2000, log_only=0):
    vvels, vlvels, vlog_par, pops = {}, {}, {}, {}
    for media in range(1, 10):
        if not log_only:
            if media not in opops.keys():
                pars = gen_pardict(g=g[media], s=s[media], growth_pars=gpars, df=10./3., m=0.5,
                model=model)
                pops[media] = analyzer(simulate_expansion(**pars).T, m=0.5, df=10./3.)
            else:
                pops[media] = opops[media]
            vvels.update({media : pops[media].velocity_threshold(thresh, pops[media].times[-20:])[0]})
        else:
            pops[media] = analyzer([[],[]], m=0.5, df=10./3.)
            vvels.update({media : 0})
        vlog_par.update({media : log(comp_fold_growth([1e-7], g[media], s[media], gpars)[0][0]/1e-7)/4.})
        vlvels.update({media : pops[media].param_logistic(g=vlog_par[media])[0]})
    return vvels, vlvels, vlog_par, pops
```

References:

1. Hewitt G (2000) The genetic legacy of the Quaternary ice ages. *Nature* 405(6789):907–913.
2. Graciá E, et al. (2013) The uncertainty of Late Pleistocene range expansions in the western Mediterranean: a case study of the colonization of south-eastern Spain by the spur-thighed tortoise, Testudo graeca. *J Biogeogr* 40(2):323–334.
3. Phillips BL, Brown GP, Greenlees M, Webb JK, Shine R (2007) Rapid expansion of the cane toad (Bufo marinus) invasion front in tropical Australia. *Austral Ecol* 32(2):169–176.
4. Veit RR, Lewis MA (1996) Dispersal, Population Growth, and the Allee Effect: Dynamics of the House Finch Invasion of Eastern North America. *Am Nat* 148(2):255–274.
5. Levine JM, D'Antonio CM (2003) Forecasting Biological Invasions with Increasing International Trade. *Conserv Biol* 17(1):322–326.
6. Pateman RM, Hill JK, Roy DB, Fox R, Thomas CD (2012) Temperature-Dependent Alterations in Host Use Drive Rapid Range Expansion in a Butterfly. *Science* 336(6084):1028–1030.
7. Walther G-R, et al. (2002) Ecological responses to recent climate change. *Nature* 416(6879):389–395.
8. Pimentel D (2014) *Biological Invasions: Economic and Environmental Costs of Alien Plant, Animal, and Microbe Species* (CRC Press).
9. Mayo JH, Straka TJ, Leonard DS (2003) The Cost of Slowing the Spread of the Gypsy Moth (Lepidoptera: Lymantriidae). *J Econ Entomol* 96(5):1448–1454.
10. Johnson DM, Liebhold AM, Tobin PC, Bjørnstad ON (2006) Allee effects and pulsed invasion by the gypsy moth. *Nature* 444(7117):361–363.
11. Sutherst RW, Floyd RB, Maywald GF (1996) The Potential Geographical Distribution of the Cane Toad, Bufo marinus L. in Australia. *Conserv Biol* 10(1):294–299.
12. Leung B, Drake JM, Lodge DM (2004) Predicting invasions: propagule pressure and the gravity of allee effects. *Ecology* 85(6):1651–1660.
13. Bocedi G, et al. (2014) RangeShifter: a platform for modelling spatial eco-evolutionary dynamics and species' responses to environmental changes. *Methods Ecol Evol* 5(4):388–396.
14. Skellam JG (1951) Random Dispersal in Theoretical Populations. *Biometrika* 38(1/2):196–218.
15. Fisher RA (1937) The Wave of Advance of Advantageous Genes. *Ann Eugen* 7(4):355–369.
16. Hanski I (1999) *Metapopulation Ecology* (OUP Oxford).
17. van Saarloos W (2003) Front propagation into unstable states. *Phys Rep* 386(2–6):29–222.
18. Murray JD ed. (1993) *Mathematical Biology* (Springer-Verlag, New York).
19. Paquette GC, Chen L-Y, Goldenfeld N, Oono Y (1994) Structural stability and renormalization group for propagating fronts. *Phys Rev Lett* 72(1):76–79.
20. Courchamp F, et al. (1999) Inverse density dependence and the Allee effect. *Trends Ecol Evol* 14(10):405–410.
21. Allee WC (1949) *Principles of Animal Ecology* (Saunders Co.).

22. Kramer AM, Dennis B, Liebhold AM, Drake JM (2009) The evidence for Allee effects. *Popul Ecol* 51(3):341–354.
23. Stephens PA, Sutherland WJ, Freckleton RP (1999) What Is the Allee Effect? *Oikos* 87(1):185–190.
24. Kot M (2001) *Elements of Mathematical Ecology* (Cambridge University Press).
25. Hallatschek O, Nelson DR (2008) Gene surfing in expanding populations. *Theor Popul Biol* 73(1):158–170.
26. Korolev KS, Avlund M, Hallatschek O, Nelson DR (2010) Genetic demixing and evolution in linear stepping stone models. *Rev Mod Phys* 82(2):1691–1718.
27. Graciá E, et al. (2013) Surfing in tortoises? Empirical signs of genetic structuring owing to range expansion. *Biol Lett* 9(3):20121091.
28. Hundertmark KJ, Daele LJV (2009) Founder effect and bottleneck signatures in an introduced, insular population of elk. *Conserv Genet* 11(1):139–147.
29. Ramachandran S, et al. (2005) Support from the relationship of genetic and geographic distance in human populations for a serial founder effect originating in Africa. *Proc Natl Acad Sci U S A* 102(44):15942–15947.
30. Lewis MA, Kareiva P (1993) Allee Dynamics and the Spread of Invading Organisms. *Theor Popul Biol* 43(2):141–158.
31. Melbourne BA, Hastings A (2009) Highly Variable Spread Rates in Replicated Biological Invasions: Fundamental Limits to Predictability. *Science* 325(5947):1536–1539.
32. Wakita J, Komatsu K, Nakahara A, Matsuyama T, Matsushita M (1994) Experimental Investigation on the Validity of Population Dynamics Approach to Bacterial Colony Formation. *J Phys Soc Jpn* 63(3):1205–1211.
33. Giometto A, Rinaldo A, Carrara F, Altermatt F (2014) Emerging predictable features of replicated biological invasion fronts. *Proc Natl Acad Sci* 111(1):297–301.
34. Jessup CM, et al. (2004) Big questions, small worlds: microbial model systems in ecology. *Trends Ecol Evol* 19(4):189–197.
35. Momeni B, Brileya KA, Fields MW, Shou W (2013) Strong inter-population cooperation leads to partner intermixing in microbial communities. *eLife* 2:e00230.
36. Ben-Jacob E, et al. (1995) Complex bacterial patterns. *Nature* 373(6515):566–567.
37. Pirt SJ (1967) A Kinetic Study of the Mode of Growth of Surface Colonies of Bacteria and Fungi. *J Gen Microbiol* 47(2):181–197.
38. Korolev KS, et al. (2012) Selective sweeps in growing microbial colonies. *Phys Biol* 9(2):26008.
39. Datta MS, Korolev KS, Cvijovic I, Dudley C, Gore J (2013) Range expansion promotes cooperation in an experimental microbial metapopulation. *Proc Natl Acad Sci* 110(18):7354–7359.
40. Korolev KS (2013) The Fate of Cooperation during Range Expansions. *PLoS Comput Biol* 9(3):e1002994.

41. Chen L, et al. (2014) Two-Dimensionality of Yeast Colony Expansion Accompanied by Pattern Formation. *PLoS Comput Biol* 10(12):e1003979.
42. Van Dyken JD, Müller MJI, Mack KML, Desai MM (2013) Spatial Population Expansion Promotes the Evolution of Cooperation in an Experimental Prisoner's Dilemma. *Curr Biol* 23(10):919–923.
43. Weber MF, Poxleitner G, Hebisch E, Frey E, Opitz M (2014) Chemical warfare and survival strategies in bacterial range expansions. *J R Soc Interface* 11(96):20140172.
44. Kerr B, Riley MA, Feldman MW, Bohannan BJM (2002) Local dispersal promotes biodiversity in a real-life game of rock–paper–scissors. *Nature* 418(6894):171–174.
45. Hallatschek O, Hersen P, Ramanathan S, Nelson DR (2007) Genetic drift at expanding frontiers promotes gene segregation. *Proc Natl Acad Sci* 104(50):19926–19930.
46. Korolev KS, Xavier JB, Nelson David R, Foster KR (2011) A Quantitative Test of Population Genetics Using Spatiogenetic Patterns in Bacterial Colonies. *Am Nat* 178(4):538–552.
47. Taylor CM, Hastings A (2005) Allee effects in biological invasions. *Ecol Lett* 8(8):895–908.
48. Keitt TH, Lewis Mark A, Holt RD (2001) Allee Effects, Invasion Pinning, and Species' Borders. *Am Nat* 157(2):203–216.
49. Gore J, Youk H, van Oudenaarden A (2009) Snowdrift game dynamics and facultative cheating in yeast. *Nature* 459(7244):253–256.
50. Dai L, Vorselen D, Korolev KS, Gore J (2012) Generic Indicators for Loss of Resilience Before a Tipping Point Leading to Population Collapse. *Science* 336(6085):1175–1177.
51. Sanchez A, Gore J (2013) Feedback between Population and Evolutionary Dynamics Determines the Fate of Social Microbial Populations. *PLoS Biol* 11(4):e1001547.
52. H. Koschwanez J, R. Foster K, W. Murray A (2011) Sucrose Utilization in Budding Yeast as a Model for the Origin of Undifferentiated Multicellularity. *PLoS Biol* 9(8):e1001122.
53. Brunet É, Derrida B (2001) Effect of Microscopic Noise on Front Propagation. *J Stat Phys* 103(1–2):269–282.
54. Brunet E, Derrida B (1997) Shift in the velocity of a front due to a cutoff. *Phys Rev E* 56(3):2597–2604.
55. Kolmogorov AN, Piscounov N, Petrowski I (1937) Étude de l'équation de la diffusion avec croissance de la quantité de matière et son application a un problème biologique. *Mosc Univ Bull Math* 1:1–25.
56. Liebhold AM, Tobin PC (2006) Growth of newly established alien populations: comparison of North American gypsy moth colonies with invasion theory. *Popul Ecol* 48(4):253–262.
57. Roques L, Garnier J, Hamel F, Klein EK (2012) Allee effect promotes diversity in traveling waves of colonization. *Proc Natl Acad Sci* 109(23):8828–8833.
58. Tobin PC, Berec L, Liebhold AM (2011) Exploiting Allee effects for managing biological invasions. *Ecol Lett* 14(6):615–624.
59. Celiker H, Gore J (2012) Competition between species can stabilize public-goods cooperation within a species. *Mol Syst Biol* 8:621.

60. Bender CM, Orszag SA (1999) *Advanced Mathematical Methods for Scientists and Engineers I* (Springer New York, New York, NY) Available at: http://link.springer.com/10.1007/978-1-4757-3069-2 [Accessed October 14, 2015].
61. Mrwebi M (2004) Testing Monod : growth rate as a function of glucose concentration in Saccharomyces cerevisiae. Thesis (Stellenbosch : University of Stellenbosch). Available at: http://scholar.sun.ac.za/handle/10019.1/16398 [Accessed January 14, 2016].
62. Vitolo M, Yassuda MT (1991) Effect of sucrose concentration on the invertase activity of intact yeast cells (S. cerevisiae). *Biotechnol Lett* 13(1):53–56.
63. Goulart AJ, et al. (2013) Glucose and Fructose Production by Saccharomyces cerevisiae Invertase Immobilized on MANAE-Agarose Support. *Rev Ciênc Farm Básica E Apl* 34(2):169–175.
64. Ben-Jacob E, Brand H, Dee G, Kramer L, Langer JS (1985) Pattern propagation in nonlinear dissipative systems. *Phys Nonlinear Phenom* 14(3):348–364.